PAPER

Heteronuclear {Tb_xEu_{1-x}} furoate 1D polymers presenting luminescent properties and SMM behavior

E.Bartolomé[a] , J. Bartolomé [b] , A. Arauzo [b,c], J. Luzón[b,d], R. Cases[b], S. Fuertes[e], V. Sicilia[f], A. I. Sánchez-Cano[g], J. Aporta[g], S. Melnic[h], D. Prodius[h,i], S. Shova[j]

We report the synthesis, crystal structure and photo-magnetic properties of novel Tb/Eu polymeric complexes of general formula {$Tb_xEu_{1-x}(\alpha\text{–fur})_3(H_2O)_3\}_n$, supported by 2-furancarboxilic acid: the homonuclear Tb(III) complex {Tb} **(1)**, four heterodinuclear complexes, {$Tb_{0.8}Eu_{0.2}$} **(2)**, {$Tb_{0.7}Eu_{0.3}$} **(3)**, {$Tb_{0.3}Eu_{0.7}$} **(4)**, {$Tb_{0.1}Eu_{0.9}$} **(5)**, and Eu(III)-only complex {Eu} **(6)**. X-ray diffraction experiments evidence that the α-furoate ligands, acting in bridging mode consolidate 1D polymeric chains along the c-axis. Luminescence studies show the sensitization capability of the furoic acid ligand. Color tuning from green to red can be successfully achieved through the heterodinuclear strategy. We have measured Eu emission by direct excitation at the resonant $^7F_0 \rightarrow {}^5L_6$ (395 nm), and indirectly, by excitation of the non-resonant wavelength (280 nm) which provokes ligand→Tb→Eu energy transfer. Besides, ac susceptibility measurements under varying frequencies and temperatures reveal that mixed {Tb_xEu_{1-x}} complexes exhibit field-induced slow relaxation dynamics, with extremely slow relaxation times, owed to direct processes affected by bottleneck effect. Thus, {Tb_xEu_{1-x}} complexes represent interesting low-dimensional multifunctional materials combining both luminescent and SMM magnetic properties.

1. Introduction

The field of molecule-based multifunctional materials has advanced quickly over recent years. Recent reports tend to focus on their fundamental qualities and potential application as molecular magnets with additional optical or electrical conductivity properties.[1] Trivalent lanthanide (Ln^{3+}) complexes are especially attractive because their unusual electronic properties make them well suited both for the construction of low-dimensional magnets[2–4] and as luminescent agents.[5–8] Within the huge family of lanthanide-based molecular magnets, Dy(III) has been the most popular ion for the synthesis of Single-Ion Magnets (SIMs)[10] and Single Molecule Magnets (SMMs).[9] Complexes based on terbium (III) non-Kramer's ion are less numerous, but with a leading importance in the field, like the first and extensively studied double-decker $[TbPc_2]^-$ SIMs,[10–13] some SMMs with record energy barriers (U_{eff}=938 K)[14], the first 3*d*–4*f* SMM ($[CuLTb(hfac)_2]_2$),[15] and complex {$[(Me_3Si)_2N]_2(THF)Tb\}_2(\mu\text{-}N_2)$[16] deploying one of the highest blocking temperatures (T_B = 14 K) within all SMMs.[16]

Works on SMMs including two different (Ln-Ln') ions are much scarcer. Among them, doping studies on triple-decker phtalocyanine[17,18] and polyoxometallates[19] heteronuclear complexes have played an important role in understanding the slow magnetic relaxation properties of dinuclear 4*f* SMMs. In addition, asymmetric dinuclear [Ln-Ln'] complexes with the two metal centres magnetically different from each other are being currently investigated as promising candidates for the realization of qugates.[20–23]

The luminescence properties of Ln(III) ions have stimulated on the other hand the investigation of novel coordination complexes with potential application in a variety of areas such as an organic light emitting diode (OLED), bioassays, contrast agents for magnetic resonance imaging etc. Lanthanides exhibit sharp emission spectra, mostly in the visible and IR range, such as green emission for Tb(III) or red emission for Eu(III). Luminescence emission arises from f-f transitions, which are well shielded from the environment by the filled 5s and 5p orbitals, and have very long-lived states. Since direct excitation of the Ln(III) cation is very weak, it must be often sensitized through a coordinated ligand acting as an "antenna". The emission intensity of the lanthanide complex is strongly dependent on the efficiency of the ligand-to-metal energy transfer, and therefore, significant efforts have been made to design ligands combining good coordinating and sensitizing properties.[7,24–26]

[a] *Escola Universitària Salesiana de Sarrià (EUSS), Passeig Sant Joan Bosco 74, 08017-Barcelona, Spain. Fax: +34 932806642; Tel: +34-932805244; E-mail: ebartolome@euss.es*
[b] *Instituto de Ciencia de Materiales de Aragón, CSIC-Universidad de Zaragoza, Pedro Cerbuna 12, 50009 Zaragoza, Spain.*
[c] *Servicio de Medidas Físicas. Universidad de Zaragoza, Pedro Cerbuna 12, 50009 Zaragoza, Spain.*
[d] *Centro Universitario de la Defensa. Academia General Militar, Zaragoza, Spain*
[e] *Departamento de Química Inorgánica, Facultad de Ciencias, Instituto de Síntesis Química y Catalisis Homogénea (ISQCH), CSIC–Universidad de Zaragoza, Spain.*
[f] *Departamento de Química Inorgánica, Escuela de Ingeniería y Arquitectura de Zaragoza, (ISQCH), Campus Río Ebro, Edificio Torres Quevedo, 50018, Zaragoza, Spain*
[g] *Depto. de Física Aplicada, Facultad de Ciencias, Universidad de Zaragoza, Spain.*
[h] *Institute of Chemistry, Academy of Sciences of Moldova, str., Academiei 3, MD-2028, Chisinau, Republic of Moldova*
[i] *Ames Laboratory, US Department of Energy and Critical Materials Institute, Ames, Iowa 50011-3020, USA*
[j] *Institute of Macromolecular Chemistry "Petru Poni" Iasi, Aleea Grigore Ghica Voda, nr. 41A, 700487 Iasi, Romania*

Electronic Supplementary Information (ESI) available: [Supplementary Information: S1. EDX and luminescence results; S2. Magnetic relaxation results]. See DOI: 10.1039/x0xx00000x

Recently, heteronuclear lanthanide-based coordination polymers are attracting much attention because of their tunable luminescent properties.[27,28] It has been demonstrated that the heterodinuclear strategy allows tuning both the emission brightness and the color. A wide range of color shades from red to green,[29–32] and from blue to green[31] were obtained in Tb/Eu complexes, while white emission has been reported in some Tb/Eu mixed complexes and Eu/Dy MOFs.[33,34] In mixed-lanthanide complexes, besides the antenna effect, energy transfer is also possible between two or more Ln ions, as observed e.g. in Y/Tb,[35] Sm/Tb[36] and Tb/Eu[26,37–40] complexes. The understanding and control of the luminescent features by effective sensitization is extremely important due to the field of application in sensors or in light-emitting diodes (LED) technology.[41]

Bifunctional Ln-based complexes exhibiting both luminescent and SMM properties are rare and limited to homonuclear complexes.[42–45] Ligand design is a key aspect to achieve bifunctionality: for SMMs, ligands with orbitals able to overlap the lanthanide 4f orbitals are desirable, whereas for luminescence, ligands that can work as efficient antennas and protect the Ln ion from vibration coupling, which may quench emission, are preferred.

Carboxyl group of 2-furoate ligand is able to mediate different magnetic couplings in light and heavy rare earth complexes.[13] We recently reported the synthesis and characterization of some one-dimensional magnets based on furoate (α-fur≡α-$C_4H_3OCOO^-$): homonuclear $\{Dy(\alpha\text{–fur})_3\}_n$[46] and $\{Tb(\alpha\text{–fur})_3\}_n$,[47] and polynuclear $\{[Ln_2Sr(\alpha\text{–fur})_8(H_2O)_4]\}_n\cdot 2H_2O$[48] and $\{[Dy_2Ba(\alpha\text{–fur})_8(H_2O)_4]\}_n\cdot 2H_2O$[49] complexes.

In the present paper we expand our efforts to the synthesis and photo-magnetic characterization of novel {Tb/Eu} α-furoate complexes of general formula $\{[Tb_xEu_{1-x}(\alpha\text{-fur})_3(H_2O)_3]\}_n$, where x=0…1, including the homonuclear {Tb}(x=1) and {Eu}(x=0) complexes and substitutional complexes with decreasing Tb/Eu ratios. We discuss in detail how the substitution of Tb by Eu ions affects the luminescence and dynamic relaxation properties of these low-dimensional magnets.

2. Experimental methods

X-ray powder diffraction: measurements were performed with a Nonius Kappa CCD diffractometer fitted with an Oxford model 700 cryostream cooler. Data were measured at 100 K using a combination of φ and ω scans with κ offsets. The data frames were integrated and scaled using the Denzo-SMN package. The structure was solved by direct methods and refined by full-matrix least squares using the software teXsan for Windows v. 1.06.

Solid state luminescent measurements: room-temperature luminescent properties under different excitation wavelengths ranging from λ_{exc}=280-400 nm, and quantum yield (QY) measurements were obtained using a Hamamatsu Absolute PL Quantum Yield spectrometer C11347 (Quantaurus QY). The absolute quantum yield (ratio of the number of photons emitted by photoluminescence to the number of photons absorbed by the light-emitting material) measurements were performed using a Jobin-Yvon integrating sphere. The absorption and emission spectra of the sample container (the blank) were recorded before measuring the powdered sample inside the same container. The QY was calculated then as: $Q = (E_c - E_a)/(L_a - L_c)$, with E_c being the integrated emission spectrum of the sample, E_a the integrated blank emission spectrum, L_a the blank absorption, and L_c the sample adsorption at the excitation wavelength.

Additional solid-state luminescent spectra were obtained in a different spectrometer equipped with a 1000 W ORIEL 66187 tungsten halogen lamp and a double 0.22 m SPEX 1680 B monochromator. Fluorescence emission was detected using a 0.5 JARREL-ASH monochromator with a Hamamatsu R928 photomultiplier tube. All optical spectroscopy measurements were corrected from the system response. Emission decay curves were obtained with the lamp beam modulated with a mechanical chopper. Lifetime measurements were carried out using a digital store oscilloscope triggered by the chopper.

Colorimetric measurements: the color coordinates determination was performed by the analysis of the emission spectra measured with the C11347 spectrometer described above. Tabulated color-matching functions $\bar{x}(\lambda)$, $\bar{y}(\lambda)$, $\bar{z}(\lambda)$ are given for computing from spectral measurements the CIE triestimulus values X, Y, Z and chromaticity coordinates x, y for the CIE 1931 standard observer 2° from 380 nm to 780 nm.[50] Primary stimuli can be calculated as $X = k\int_\lambda I(\lambda)\bar{x}(\lambda)d\lambda$, $Y = k\int_\lambda I(\lambda)\bar{y}(\lambda)d\lambda$, $Z = k\int_\lambda I(\lambda)\bar{z}(\lambda)d\lambda$,with $k = 100/\int_\lambda I(\lambda)\bar{y}(\lambda)d\lambda$, where $I(\lambda)$ is the spectral power of the luminescence decays measured with the spectrometer. Chromaticity coordinates x, y were obtained by dividing each triestimulus value X, Y, Z by the sum of all three, $x = X/(X+Y+Z); y = Y/(X+Y+Z)$.

Magnetometry: dc and ac susceptibility of powdered samples were measured, above 1.8 K, using a Quantum Design superconducting quantum interference device (SQUID) magnetometer. Ac measurements were done at an excitation field of 4 Oe, and under dc fields between 0-20 kOe, while sweeping the frequency between 0.01 and 1000 Hz. Measurements on powdered samples were performed with the addition of Daphne oil, introduced to fix the grains at low temperatures.

Heat capacity: $C(T)$ under different applied fields (0-4 kOe) was measured on a pressed powder pellet fixed with Apiezon N grease to assure good thermal contact, using a Quantum Design PPMS.

3. Synthesis

The rational design of specific clusters with two different lanthanides in a monocrystal and characteristic luminescence is still a challenge for chemists. Herein we report an original method for the preparation of these lanthanide complexes. All manipulations were performed under aerobic conditions. All chemicals were used as received. $\{[Ln_2Sr(\alpha\text{-fur})_8(H_2O)_4]\}_n\cdot 2H_2O$ were available from previous work. Two general protocols were applied for the preparation of homo and heteronuclear complexes.

Method A. An aqueous solution (10 ml) of magnesium(II) furoate (0.5 mmol) was added to an ethanol solution (10 ml) of lanthanide(III) perchlorate (0.5 mmol) with constant stirring for 20 min until the solution becomes transparent. After a week colorless crystals were collected, washed with ethanol and dried under vacuum. Later on we found that heteronuclear compounds can be obtained more conveniently by method B.

CAUTION: Perchlorate salts of metal complexes with organic ligands are potentially explosive and must be handled with caution.

Method B. To a stirred solution of $\{[Ln_2Sr(\alpha\text{-fur})_8(H_2O)_4]\}_n\cdot 2H_2O$ in H_2O (15 ml) a colorless solution of lanthanide(II) sulfate was added. The resulting solution with a precipitate of strontium(II) sulfate was

stirred for 30 min and filtered and the filtrate was left undisturbed to concentrate slowly by evaporation. After about one week, well-shaped crystals were collected by filtration, washed with ethanol and dried under vacuum. The identity of the products was confirmed by elemental analysis (C, H) and IR spectroscopic comparison with materials from method A.

Despite the identity of the obtained results and affiliation with exchange (ligand-to-ligand for method A and metal-to-metal for method B) reactions, they have some conceptual differences. First of all, in case of method A, we can see the formation of thermodynamically favorable Ln(III) furoate complex derived from the straightforward mixing of corresponding salts in aqueous solution. This is not the case for method B, where we constrain metal-to-metal exchange (Sr^{2+} to Ln^{3+}) through the separation of insoluble product, strontium(II) sulfate. A similar synthetic strategy was successfully applied for the exchange transformation from the μ_3-oxo $\{Fe_2Ba\}$ carboxylates[51] to the novel "butterfly"-like SMMs family[52–57] based on the first example of iron-lanthanide carboxylate.[52] Finally, the method A is a less favorable route than method B because of the safety issues associated with hazardous work with explosives.

$\{Tb(\alpha\text{-fur})_3(H_2O)_3\}_n$, abbreviated {Tb}(1)
The synthesis of **(1)** by method A was previously reported.[49] The same result was obtained by method B when we used as precursor $\{[Tb_2Sr(\alpha\text{-fur})_8(H_2O)_4]\}_n{\cdot}2H_2O$[58] (0.420 g, 0.3 mmol) and $Tb_2(SO_4)_3{\cdot}8H_2O$ (0.075 g, 0.1 mmol). White crystals were obtained in ca. 80% yield. Calc. for $(TbO_{12}C_{15}H_{15})_n$: C, 32.98; H, 2.77;. Found: C, 32.91; H, 2.78; IR (cm^{-1}): 3120b, 1583sh, 1564b, 1471s, 1413s, 1399b, 1230m, 1199s, 1136m, 1074m, 1013m, 932m, 883m, 785b, 759b.

$\{Tb_{0.8}Eu_{0.2}(\alpha\text{-fur})_3(H_2O)_3\}_n$, abbreviated $\{Tb_{0.8}Eu_{0.2}\}$(2)
This complex was prepared by method A, using the respective ratio of the initial perchlorate salts, $Eu(ClO_4)_3{\cdot}8H_2O$ (0.40 mmol) and $Tb(ClO_4)_3{\cdot}8H_2O$ (0.10 mmol). White crystals were obtained in ca. 80% yield. Calc. for $(C_{15}H_{15}O_{12}Eu_{0.2}Tb_{0.8})_n$: C, 33.07; H, 2.77; Found: C, 33.10; H, 2.82; IR (cm^{-1}): 3072b, 1583sh, 1544b, 1474s, 1417s, 1368b, 1232m, 1196s, 1136m, 1076m, 1010m, 934m, 884m, 784b, 766b.

$\{Tb_{0.7}Eu_{0.3}(\alpha\text{-fur})_3(H_2O)_3\}_n$, abbreviated $\{Tb_{0.7}Eu_{0.3}\}$(3)
This complex was prepared by method B, used as precursors $\{[Tb_2Sr(\alpha\text{-fur})_8(H_2O)_4]\}_n{\cdot}2H_2O$ (0.420 g, 0.3 mmol) and $Eu_2(SO_4)_3{\cdot}8H_2O$ (0.074 g, 0.1 mmol). White crystals were obtained in ca. 85% yield. Calc. For $(C_{15}H_{15}O_{12}Eu_{0.33}Tb_{0.67})_n$: C, 33.13; H, 2.78; Found: C, 33.11; H, 2.88; IR (cm^{-1}): 3120b, 1584sh, 1541b, 1472s, 1417s, 1368b, 1233m, 1200s, 1136m, 1077m, 1010m, 936m, 885m, 784b, 767b.

$\{Tb_{0.3}Eu_{0.7}(\alpha\text{-fur})_3(H_2O)_3\}_n$, abbreviated $\{Tb_{0.3}Eu_{0.7}\}$(4)
This complex was prepared by method B, used as precursors $\{[Eu_2Sr(\alpha\text{-fur})_8(H_2O)_4]\}_n{\cdot}2H_2O$ (0.416 g, 0.3 mmol) and $Tb_2(SO_4)_3{\cdot}8H_2O$ (0.075 g, 0.1 mmol). White crystals were obtained in ca. 85% yield. Cal. for $(C_{15}H_{15}O_{12}Eu_{0.67}Tb_{0.33})_n$: C, 33.28; H, 2.79; Found: C, 33.21; H, 2.75; IR (cm^{-1}): 3120b, 1584sh, 1541b, 1472s, 1417b, 1367b, 1234w, 1200s, 1137m, 1077w, 1010m, 936m, 884m, 784b, 767b.

$\{Tb_{0.1}Eu_{0.9}(\alpha\text{-fur})_3(H_2O)_3\}_n$, abbreviated $\{Tb_{0.1}Eu_{0.9}\}$ (5)
This magnetically diluted powder sample was prepared by method A, using the respective ratio of the initial salts $Eu(ClO_4)_3{\cdot}8H_2O$ (0.45 mmol) and $Tb(ClO_4)_3{\cdot}8H_2O$ (0.05 mmol). White crystals were obtained in ca. 80% yield. Calc. for $(C_{15}H_{15}O_{12}Eu_{0.9}Tb_{0.1})_n$: C, 33.37; H, 2.80; Found: C, 33.31; H, 2.78; IR (cm^{-1}): 3119b, 1583sh, 1541b, 1471s, 1417s, 1368b, 1233m, 1199s, 1136m, 1076m, 1010m, 935m, 885m, 785b, 767b.

$\{Eu(\alpha\text{-fur})_3(H_2O)_3\}_n$, abbreviated as {Eu} (6)
This was prepared by method A, using as precursors magnesium(II) furoate (0.5 mmol) and $Eu(ClO_4)_3{\cdot}8H_2O$ (0.5 mmol). White crystals were obtained in ca. 80% yield. Calc. for $(C_{15}H_{15}O_{12}Eu)_n$: C, 33.41; H, 2.80; Found: C, 33.38; H, 2.78; IR (cm^{-1}): 3119b, 1583sh, 1544b, 1473s, 1419s, 1368b, 1233m, 1199s, 1136m, 1076m, 1010m, 935m, 884m, 785b, 767b.

EDX analysis: Energy-dispersive X-ray spectroscopy (EDX) analysis was used to investigate the composition of the samples. Fig. S3 (left) shows e.g. a broad-area EDX spectrum of the synthesized complex **(4)**. The expected emission lines from Eu and Tb were apparent in the figures, indicating the presence of Tb and Eu in the complex. The relative integrated intensity of appropriate pairs of Tb and Eu emission lines allowed the calculation of the Tb/Eu atomic ratio. This

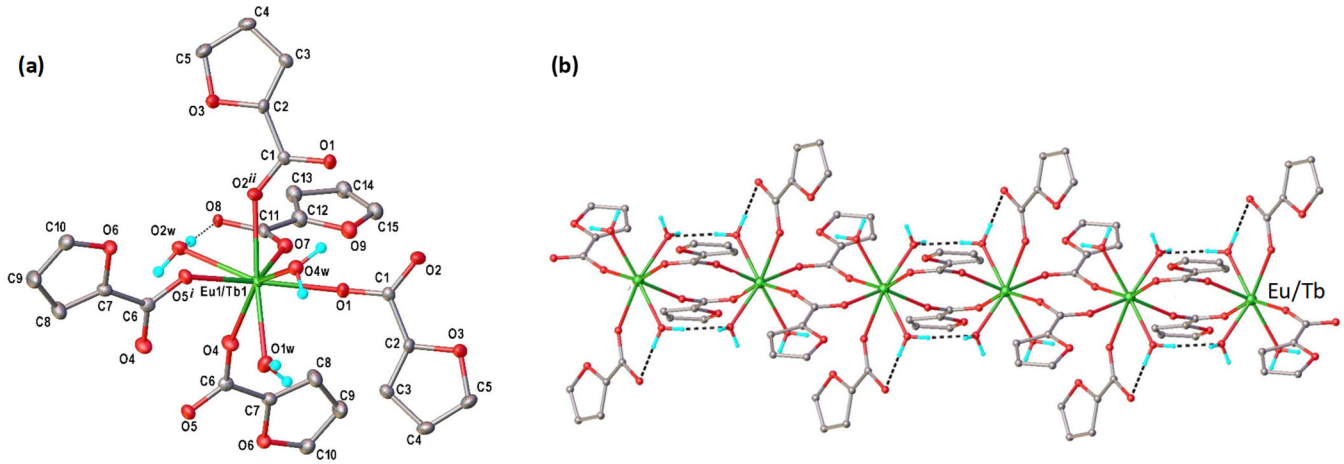

Fig. 1. (a) Extended asymmetric unit in the crystal structure of $\{Tb_xEu_{1-x}(\alpha\text{–fur})_3(H_2O)_3\}_n$ with atom labeling scheme and thermal ellipsoids at 50% probability level. Symmetry codes: [i] 0.5 – *x*, 0.5 – *y*, 2 – *z*; [ii] 0.5 – *x*, 0.5 – *y*, 1 – *z*. H-bond parameters: O2*w*-H···O8 [O2*w*-H 0.834 Å, H···O8 1.774 Å, O2*w*···O8 2.603(8) Å, ∠ O2*w*-H···O8 172.7 °; (b) stoichiometric random distribution of Tb-Eu atoms along the 1D polymeric parallel to the *c*-axis.

analysis demonstrates that we were successful in synthesizing mixed-lanthanide compounds where europium and terbium are equally incorporated into the crystal structure. This is not entirely unexpected since these lanthanides do not vary considerably in their ionic radii.

4. Structural characterization

Compounds **1-6** form a series of isomorphous coordination polymers with the general formula $\{Tb_xEu_{1-x}(\alpha\text{-fur})_3(H_2O)_3\}_n$, with α-fur=C_4H_3OCOO. Table 1 provides a summary of the crystallographic data together with refinement details for compounds **1-6**. CCDC 1438521 **(3)**, CCDC-1438520 **(4)** and CCDC-1438519 **(6)** contain the supplementary crystallographic data for this contribution. Compounds **(2, 5)** are isostructural to the mentioned complexes, which was confirmed by X-ray powder diffraction analysis (Fig. S2). Selected interatomic distances are listed in Table 2.

The main structural features of **2-6** are similar to those of previously reported complex **(1)**.[47] We summarize here the principal structural characteristics, and focus on the particularities introduced by the substitution of Tb by Eu in the heterocomplexes. The Eu substitutes Tb randomly in the crystal lattice. The coordination polyhedron of each Ln=Tb, Eu can be described as a distorted bicapped trigonal prism (Fig. 1a and Fig. S1).

Each Ln is coordinated by eight oxygen atoms: four oxygen atoms from two pairs of α-furoates in bridging mode coordinating with neighbor Ln atoms, one oxygen atom originating from a deprotonated monodentate α-furoate ligand and three water molecules. One of the α-furoate ligand was found to be disordered into two resolvable positions with equal probability, so each lanthanide exhibits two different but very similar coordination environments of lanthanide atoms (Fig. S1). *Ab initio* calculations

Table 2. Selected bond distances (Å) for **3, 4** and **6**.

	3 (M= Tb/Eu)	**4** (M=Tb/Eu)	**6** (M=Eu)
M1-O1	2.326(3)	2.320(3)	2.354(5)
M1-O1*w*	2.424(3)	2.412(3)	2.559(4)
M1-O2[1]	2.347(3)	2.340(3)	2.327(4)
M1-O2*w*	2.564(3)	2.547(3)	2.425(4)
M1-O3*w*	2.500(6)	2.502(9)	2.478(13)
M1-O4*w*	2.491(8)	2.407(8)	2.450(12)
M1-O4	2.306(3)	2.303(3)	2.381(4)
M1-O5[2]	2.378(3)	2.369(3)	2.328(5)
M1-O7x	2.417(8)	2.492(9)	2.413(13)
M1-O7	2.407(6)	2.375(9)	2.466(12)
O1-C1	1.250(5)	1.253(5)	1.256(7)
O2-C1	1.246(5)	1.252(5)	1.252(7)
O3-C2	1.372(5)	1.368(5)	1.376(7)
O3-C5	1.362(6)	1.363(5)	1.356(8)
O4-C6	1.253(5)	1.256(5)	1.252(8)
O5-C6	1.260(5)	1.250(5)	1.257(8)
O6-C7	1.365(5)	1.362(5)	1.365(8)
O6-C10	1.365(6)	1.353(5)	1.352(7)
O8-C11	1.269(7)	1.266(12)	1.287(14)

Symmetry codes: [1)] $0.5-x, 0.5-y, 2-z$; [2)] $0.5-x, 0.5-y, 1-z$.

Table 1. Crystallographic data, details of data collection and structure refinement parameters for {Tb} **(1)**,[47] $\{Tb_{0.7}Eu_{0.3}\}$ **(3)**, $\{Tb_{0.3}Eu_{0.7}\}$ **(4)** and homonuclear {Eu} **(6)**.

Complex	**1**	**3**	**4**	**6**
CCDC	1438518	1438521	1438520	1438519
Empirical formula	$C_{15}H_{15}O_{12}Tb$	$C_{15}H_{15}O_{12}Eu_{0.33}Tb_{0.67}$	$C_{15}H_{15}O_{12}Eu_{0.67}Tb_{0.33}$	$C_{15}H_{15}O_{12}Eu$
Formula weight	546.19	543.87	541.32	539.23
Temperature/K	293	293	100	160
Crystal system	monoclinic	monoclinic	monoclinic	monoclinic
Space group	*C*2/*c*	*C*2/*c*	*C*2/*c*	*C*2/*c*
a/Å	22.1451(8)	22.1778(6)	21.985(8)	22.0253(17)
b/Å	16.0302(6)	16.0639(4)	15.883(6)	15.9315(9)
c/Å	10.2110(4)	10.2487(3)	10.192(4)	10.2459(7)
α/°	90.00	90.00	90.00	90.00
β/°	100.040(4)	100.134(2)	100.172(6)	100.064(7)
γ/°	90.00	90.00	90.00	90.00
V/Å^3	3569.3(2)	3594.27(15)	3503(2)	3539.9(4)
Z	8	8	8	8
D_{calc}/mg/mm^3	2.033	2.010	2.053	2.024
μ/mm^{-1}	4.028	3.852	3.785	3.610
Crystal size/mm^3	0.50 × 0.20 × 0.20	0.40 × 0.40 × 0.05	0.34 × 0.29 × 0.14	0.80 × 0.20 × 0.15
ϑ_{min}, ϑ_{max}(°)	3.16 to 50.04	6.14 to 50.06	4.88 to 50.04	3.18 to 48.8
Reflections collected	6723	7528	8880	6257
Independent reflections	3144 [R_{int} = 0.0439]	3164 [R_{int} = 0.0190]	3043 [R_{int} = 0.0197]	2897 [R_{int} = 0.0429]
Data/restraints/parameters	3144/108/235	3164/7/284	3043/1/241	2897/8/226
GOF[c]	1.073	1080	1.033	1.091
R_1[a]($I>2\sigma(I)$)	0.0396	0.0280	0.0278	0.0411
wR_2[b](all data)	0.0989	0.0687	0.0648	0.0938
Largest diff. peak/hole/e Å^{-3}	0.85/-0.84	0.71/-0.85	0.82/-1.00	1.96/-1.68

[a] $R_1 = \Sigma||F_o| - |F_c||/\Sigma|F_o|$, [b] $wR_2 = \{\Sigma[w(F_o^2 - F_c^2)^2]/\Sigma[w(F_o^2)^2]\}^{1/2}$.

[c] GOF = $\{\Sigma[w(F_o^2 - F_c^2)^2]/(n-p)\}^{1/2}$, where n is the number of reflections and p is the total number of parameters refined .

earlier reported for homonuclear complex **1** showed that for both sites, Tb(A) and Tb(B), the magnetic ground state is highly anisotropic (g_z*=17.8) and consists of a "quasi-doublet" with a small gap (Δ_A/k_B = 0.201 K and Δ_B/k_B = 0.258 K), well isolated from the next excited state, at E_{2A}/k_B = 185.9 K and E_{2B}/k_B = 168.8 K for sites A and B, respectively[47].

The α-furoate bridging ligands form 1D polymeric chains of Tb/Eu ions of the same type (either A or B) running along the *c*-axis. In the heteronuclear complexes a random distribution of Tb and Eu atoms in ratio x:1-x can be found in the chain (Fig. 1b). The crystal structure is formed by the supramolecular stacking along the *a*-axis of 2D layers containing parallel chains of the same type[47]. The Ln···Ln separation in the *a* and *b* directions ranges from 10.75 to 11.27 Å and from 7.95 to 8.04 Å, respectively. Due to the polymeric character of the complexes, defects within the chains, *bc* planes and along the packing in the *a*-direction may be anticipated.

5. Luminescent properties

When exposed under UV radiation all complexes emit visible light (Fig. S3, right). Quantitative luminescence studies at room temperature were conducted on samples **1-6** in order to assess the *ligand→Tb(III)→Eu(III)* energy transfer, luminescence relaxation lifetimes and characterize the colorimetric properties.

First, the excitation spectra of the pure systems {Tb} and {Eu} were measured to determine the optimum wavelengths of excitation of these compounds (Fig. 2). The excitation spectra show broad bands from the furoic ligand below 300 and 350 nm, respectively, with a maximum absorption at around 280 nm, which was thereafter the chosen wavelength for emission studies upon ligand excitation. Besides, sharp lines corresponding to the lanthanide excitation are observed, among which the direct Tb excitation $^7F_6 \rightarrow {}^5D_3$ at 380 nm and Eu excitation $^7F_0 \rightarrow {}^5L_6$ at 395 nm. In the case of {Tb}, the intensity of the ligand band is larger than that of the Tb (380 nm) peak ("antenna effect") (Fig. 2a), while for the {Eu} complex the excitation intensities of the band and the Eu (395 nm) peak are similar (Fig. 2b).

The emission spectra for each compound were measured upon non-resonant ligand excitation at 280 nm (Fig. 3), and upon direct resonant excitation of each one of the lanthanides. The spectra under direct 395 nm excitation for the Eu complex, and under 380 nm for the Tb-containing complexes can be found in Fig. S4 and Fig. S5, respectively.

Luminescence lifetime, on the other hand, have been obtained only under direct excitation, since it allows obtaining relaxation times closer to intrinsic times and avoid non-desired decays from higher levels that could interfere in the results. In the case of Tb^{3+} the $^5D_4$ emitting level was excited (λ_{ex}= 487 nm) (see Fig. 5). In the Eu^{3+} we have excited to the $^5D_1$ level (λ_{ex}= 526 nm) which is very close in energy to the emitting $^5D_0$ level and the energy decays non-radiatively to $^5D_0$ level. In this case, direct excitation to $^5D_0$ has been ruled out due to the low absorption of the transition $^7F_0$ -> $^5D_0$ which is practically forbidden. Transfer energy effects from the ion under study are easily discerned in this way.

.

Luminescence from homonuclear {Tb} and {Eu} complexes: The emission spectrum of the {Tb} compound when excited at λ_{exc} = 280 nm exhibits four characteristic bands at 487, 546, 590 and 616 nm, which correspond to $^5D_4 \rightarrow {}^7F_J$ (J=6, 5, 4, 3) transitions to the ground state multiplet of the Tb(III) ion (Fig. 3), and is dominated by the $^5D_4 \rightarrow {}^7F_5$ transition at 546 nm. The luminescence lifetime of this peak, when the Tb^{3+} is excited directly at the $^5D_4$ level (487 nm), is τ_{obs}^{Tb} =0.82 ms. (see Table 3 and Fig. S6). The overall quantum yield upon ligand excitation (280 nm), Q_{Tb}^{ligand}, was found to be sizeable (23.8%), and notably, larger than the intrinsic quantum yield upon direct excitation of the Tb ion (380 nm), Q_{Tb}^{Tb} =12.8%.

The sensitization efficiency (η_{sens}^{Ln}) is defined as the efficacy with which energy is transferred from the feeding levels of the metal-ion surroundings onto the Ln^{III} excited state:

$$Q_{Ln}^{ligand} = \eta_{sens}^{Ln} \times Q_{Ln}^{Ln} = \eta_{sens}^{Ln} \times \frac{\tau_{obs}^{Ln}}{\tau_{rad}^{Ln}}, \qquad [1]$$

where τ_{obs}^{Ln} is the observed luminescent lifetime, and τ_{rad}^{Ln} the radiative luminescent lifetime. The large value obtained η_{sens}^{Tb} =186% indicates that furoic ligand is a good sensitizer for the Tb ion in the pure complex {Tb}.

The emission spectrum under direct Eu excitation (395 nm), recorded with a higher energy resolution spectrometer (Fig. S4b) allows observing the presence of the transition $^5D_0 \rightarrow {}^7F_0$ (579.5 nm), which indicates the absence of an inversion centre (the point symmetry of Eu sites is C_2, a binary axis parallel to the *b*-axis). A single peak is observed, demonstrating that the two nearest neighbor coordination environments, Ln(A) and Ln(B), owing to the different position of the α-fur capping ligand as obtained by X-ray diffraction,

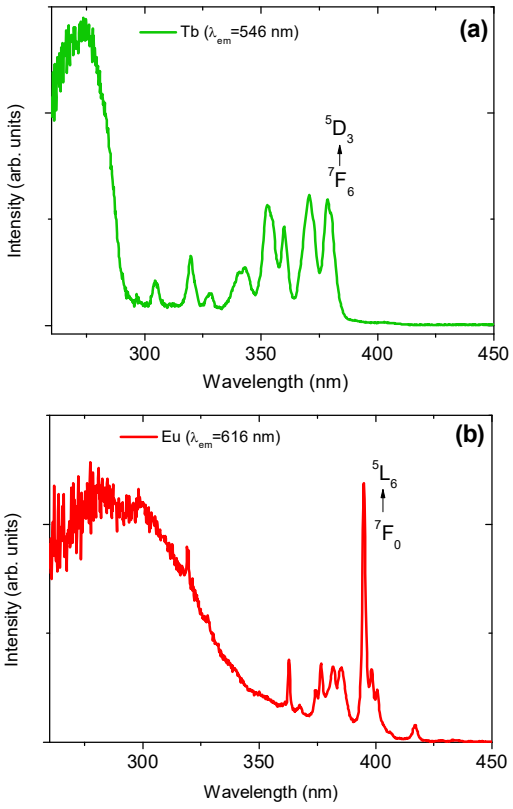

Fig. 2. Room-temperature excitation spectra of complexes: (a) {Tb} with emission monitored at λ_{em}=546 nm, and (b) {Eu} at λ_{em}=616 nm.

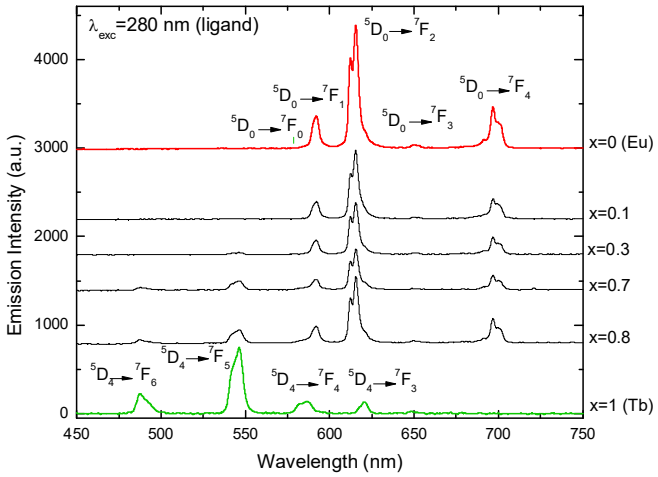

Fig. 3. Emission spectra of {Tb_xEu_{1-x}}, x=0, 0.1, 0.3, 0.7, 0.8, 1 compounds, excited at λ_{exc}=280 nm.

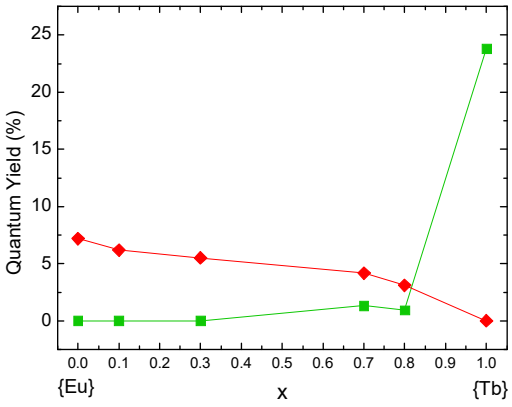

Fig. 4. Quantum yield Q_{Tb}^{ligand} (in green) and Q_{Eu}^{ligand} (in red) versus x for {Tb_xEu_{1-x}}, x=0, 0.1, 0.3, 0.7, 0.8, 1 compounds, excited at λ_{exc}=280 nm; Quantum yields determined with a relative error <10%.

are practically identical. The ratio between the intensity of the hypersensitive electric-dipole transition $^5D_0 \rightarrow {}^7F_2$ (hypersensitive to the coordination environment) and that of the magnetic dipole transition $^5D_0 \rightarrow {}^7F_1$ is rather large, I($^5D_0 \rightarrow {}^7F_2$)/I($^5D_0 \rightarrow {}^7F_1$)=3.8, which is in agreement with the relatively low symmetry of the Ln sites.[59]

The emission spectrum of the pure {Eu} complex when excited at the ligand λ_{exc}=280 nm displays typical Eu^{3+} transitions $^5D_0 \rightarrow {}^7F_J$, where one observes those for J=0-4, and is dominated by the transition $^5D_0 \rightarrow {}^7F_2$ centered at 616 nm (Fig. 3). The luminescence relaxation time decay of this peak, when Eu^{3+} is excited at the $^5D_1$ level (526 nm), is τ_{obs}^{Eu} =0.27 ms. (see Table 3 and Fig. S6).

The total quantum yield upon ligand excitation Q_{Eu}^{ligand} =7.3% is almost identical to the intrinsic quantum yield upon Eu excitation, Q_{Eu}^{Eu} =7.1%, so the sensitization efficiency is large η_{sens}^{Eu} ≈100%. Note that Q_{Eu}^{Eu} is not much smaller than Q_{Tb}^{Tb}, different than in other reported compounds, where non-radiative deactivation of the Eu^{3+} is important[31].

Luminescence from heteronuclear complexes {Tb_xEu_{1-x}}: Under excitation at 280 nm of the ligand, the emission spectra of the mixed compounds show five major peaks at 487, 546, 590, 616 and 698 nm (Fig. 3), resulting from the Tb and Eu emissions. As the ratio of Eu/Tb ions increases, the intensity of the Eu peaks $^5D_0 \longrightarrow {}^7F_{1\text{-}4}$ increases, while that of Tb peaks $^5D_4 \rightarrow {}^7F_{3-6}$ decreases. In the most diluted complexes studied, with x=0.1, 0.3, Tb emission peaks are practically quenched.

On the other hand, note that in complex {$Tb_{0.8}Eu_{0.2}$}, with only a 20% substitution of Tb ions by Eu, the intensity of the Tb peak is very low. Moreover, the relaxation of this peak is very fast and non-exponential. Simultaneously, very strong Eu emission peaks are induced. The relaxation time of the main Eu peak (616 nm) is equal to 0.32 ms, slightly larger than that of the pure sample {Eu}. These features indicate the presence of a very effective intermetallic Tb-to-Eu energy transfer.

Table 3. Spectroscopic data for Tb/Eu complexes **1-6**. r_{Tb}(r_{Eu})relative contribution of Tb(Eu), respectively, to measured total quantum yield; intrinsic quantum yields Q_{Eu}^{Eu} and Q_{Tb}^{Tb} have been estimated on the basis of emission spectra recorded when excited at 395 nm ($^5L_6$energy level for Eu^{3+}) and 380 nm ($^5D_3$ energy level for Tb^{3+}), respectively; the relative errors in QY are <10%; τ_{obs}^{Tb} observed luminescent relaxation time of Tb peak (546 nm) when excited at 487 nm; τ_{obs}^{Eu} observed luminescent relaxation time of Eu peak (616 nm) when excited at 526 nm; * Non-exponential, very fast relaxation.

Complex	x	r_{Tb} (%)	r_{Eu} (%)	Q_{Tb}^{ligand} (%)	Q_{Eu}^{ligand} (%)	Q_{Ln}^{Ln} (%)	τ_{obs}^{Tb} (ms)	τ_{rad}^{Tb} (ms)	τ_{obs}^{Eu} (ms)	τ_{rad}^{Eu} (ms)	η_{sens}^{Tb} (%)	η_{sens}^{Eu} (%)	η_{ET} (%)
{Tb}	1	100	0	23.8	_	12.8	0.82	6.41	_	_	186	_	
{$Tb_{0.8}Eu_{0.2}$}	0.8	22.9	77.0	0.92	3.11	_	0.17-0.29	*	0.32	4.24	25.5	41.2	64-79
{$Tb_{0.7}Eu_{0.3}$}	0.7	24.0	75.9	1.33	4.20	_	*	*	0.31	4.24	*	57.5	
{$Tb_{0.3}Eu_{0.7}$}	0.3	0	100	_	5.52	_	*	*	0.29	4.24	*	80.7	
{$Tb_{0.1}Eu_{0.9}$}	0.1	0	100	_	6.19	_	*	*	0.28	4.24	*	95.2	
{Eu}	0	0	100	_	7.3	7.2	_	_	0.27	4.24	_	101	

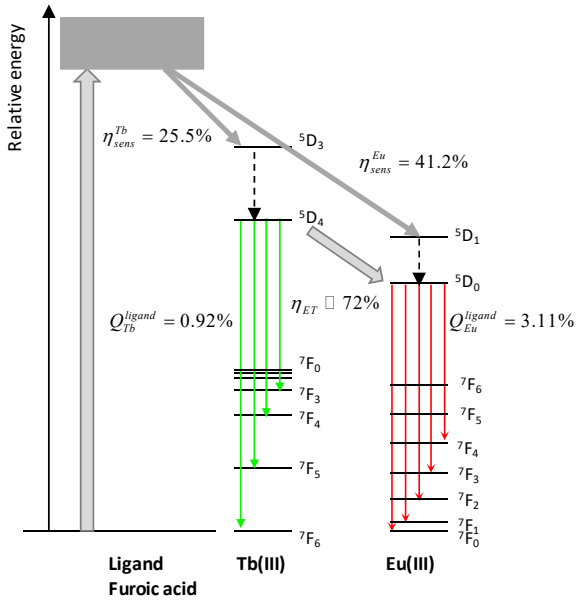

Fig. 5. Schematic energy transfer diagram suggested for the {Tb/Eu} mixed complexes (e.g. quantum yield and sensitization efficiency values for complex $\{Tb_{0.8}Eu_{0.2}\}$ are given). Dotted arrows denote non-radiative deactivation.

The quantum yield contributions Q_{Tb}^{ligand} and Q_{Eu}^{ligand} in the mixed compounds have been estimated from the total quantum yield, considering the relative intensities r_{Tb} and r_{Eu} ($Q_{Ln}^{ligand} = r_{Ln} \cdot Q_{Total}^{ligand}$) given in Table 3. Figure 4 shows the evolution of Q_{Tb}^{ligand} and Q_{Eu}^{ligand} as a function of x. It is observed that the intrinsic quantum yield upon ligand excitation of Tb is abruptly reduced as soon as some Tb ions

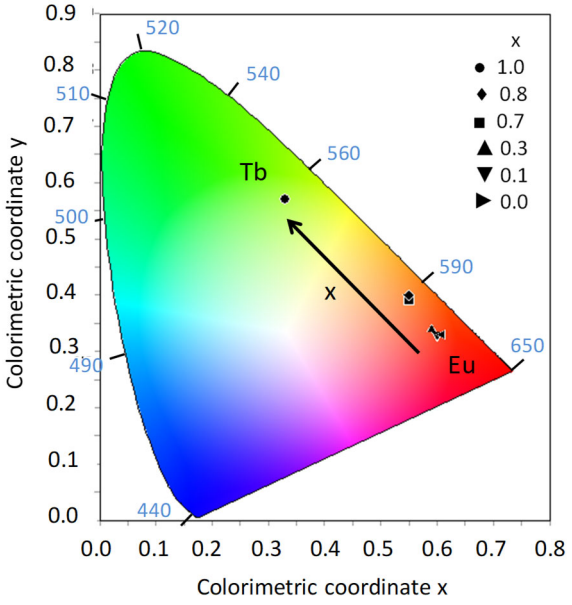

Fig. 6. Colorimetric coordinates for the $\{Tb_xEu_{1-x}\}$, x=0, 0.1, 0.3, 0.7, 0.8, 1 compounds measured under λ_{exc}=280 nm ligand excitation (coordinate values are given in Fig. S4).

Table 4. Total quantum yields measured at λ_{exc}=280 nm (ligand), λ_{exc}=380 nm (Tb), λ_{exc}=395 nm (Eu) excitation. For λ_{exc}=380 nm excitation, the partial Tb and Eu contributions, Q_{Tb}^{Tb} and Q_{Eu}^{Eu}, to the total quantum yield Q_{Total}^{Tb} are given; the relative errors in QY are <10%.

x	Q_{Total}^{ligand} (%) 280 nm	Q_{Total}^{Tb} (%) 380 nm	Q_{Tb}^{Tb} (%) 380 nm	Q_{Eu}^{Tb} (%) 380 nm	Q_{Total}^{Eu} (%) 395 nm
1	23.8	12.76	12.76	_	0
0.8	4.04	1.48	0.69	0.79	0.6
0.7	5.53	2.39	0.67	1.72	1.29
0.3	5.52	1.79	_	1.79	1.07
0.1	6.19	4.87	_	4.87	7.8
0	7.21	4.06	7.1	4.06	7.07

are substituted by Eu (Q_{Tb}^{ligand} =0.92% for x=0.8), while Eu quantum yield Q_{Eu}^{ligand} (x) decreases only moderately (Q_{Eu}^{ligand} =6.19% for x=0.1).

The sensitization efficiency (η_{sens}^{Ln}) relative to the Tb and Eu ions can be estimated with Eq. [1], under the assumption that radiative lifetimes of the homonuclear complexes are a good approximation of the radiative lifetimes τ_{rad}^{Ln} of all the isostructural Tb/Eu compounds[31]. The sensitization efficiency relative to Eu η_{sens}^{Eu} of the different mixed complexes reached η_{sens}^{Eu} ≈41-95% for Tb contents ranging from x=0.8-0.1. The sensitization of the Eu ion in the mixed compounds is smaller than for pure {Eu}, but still sizeable, even for the $\{Tb_{0.8}Eu_{0.2}\}$ complex. On the other hand the luminescence relaxation time of Tb was difficult to quantify, given the non-exponential and extremely rapid decay of the 546 nm peak in the mixed compounds, hindering the determination of τ_{rad}^{Tb} and η_{sens}^{Tb}. For the $\{Tb_{0.8}Eu_{0.2}\}$, the relaxation presented a two-slope decay, with a relaxation time between τ_{obs}^{Tb} ~0.17-0.29 ms, from which a sensitization efficiency relative to Tb η_{sens}^{Tb} ~25.5% is estimated, significantly smaller than that of the pure complex.

The intermetallic energy transfer (η_{ET}) in the mixed complexes can be quantified using the relationship:

$$\eta_{ET} \approx 1 - \frac{\tau_{obs}}{\tau_0}, \qquad [2]$$

where $\tau_{obs} = \tau_{obs}^{Tb}\{Tb_xEu_{x-1}\}$ and $\tau_0 \approx \tau_{obs}^{Tb}\{Tb\}$ are, respectively the lifetimes in the presence and in the absence of an acceptor[60]. For the $\{Tb_{0.8}Eu_{0.2}\}$ complex, the energy transfer is estimated to be η_{ET} ~64-79%.

Summing up, our study allows establishing that there is ligand to metal energy transfer, probably by ligand-to-metal charge transfer state (LMCT), and clearly an energy transfer from Tb to Eu in mixed samples **(2-5)**, which is practically complete for Tb substitution by Eu larger than 20%. The energy transfer diagram suggested for the mixed complexes is schematized in Figure 5.

The total quantum yield of all complexes measured under ligand excitation (280 nm) compared to those measured under Tb (380 nm) and Eu (395 nm) excitation are given in Table 4. When exciting under 395 nm, only Eu^{3+} direct process is addressed. Therefore the

quantum yield for direct excitation at Eu^{3+}, gives a measurement of the effect of mixed compounds on the fluorescence efficiency of Eu^{3+} without involving intermetallic energy transfer.

When exciting at 380 nm, both Tb^{3+} and Eu^{3+} direct excitation is produced. As can be observed in Table 4, direct excitation of Eu^{3+} is less efficient at 380 nm than at 395 nm in the Eu pure complex. However, $Tb^{3+}\rightarrow Eu^{3+}$ energy transfer increases the quantum yield of direct excitation of Eu^{3+} at 380 nm in mixed compounds as compared to direct excitation of Eu^{3+} energy levels at 395 nm.

Colorimetric measurements performed under λ_{exc}=280 nm are shown in Figure 6. Color tuning from green-to-red emission is observed for the $\{Tb_xEu_{1-x}\}$ compounds, with a rapid evolution towards reddish coordinates for decreasing x. Non-linear colorimetric properties as a function of the Tb/Eu contents have been previously reported.[31,61,62] Besides, the color coordinates shift as a function of the excitation wavelength, as shown by the colorimetric measurements for the samples excited at λ_{exc}=380 nm ($^5D_3$ energy level for Tb^{3+}) (Fig. S8). Thus, color emission can be tuned adjusting the relative concentration of Tb/Eu ions and the excitation wavelength.

To end with, we discuss briefly the luminescent properties of our Tb/Eu complexes compared with others reported in the literature (see Table S1). To achieve an efficient antenna effect, a multitude of organic ligands bearing aromatic chromophores have been proposed, derived e.g. from bipyridine, terpyridine, triphenylene, quinoline or substituted phenyl and naphthyl groups.[5] The α-furoate ligand, including a cyclic pentagon with 4C and 1O, has demonstrated to be an efficient antenna group. The sensitization factor of the pure complex {Tb}, η_{sens}^{Tb} ~186%, is one of the highest reported. On the other hand, the obtained quantum yields upon ligand excitation for the pure {Tb} and {Eu} complexes are rather typical, with values Q_{Tb}^{ligand} =23.8% (Q_{Eu}^{ligand} =7.3%) within ranges commonly reported, Q_{Tb}^{ligand} =24-45.58% (Q_{Eu}^{ligand} =7.7-14%), respectively. Regarding energy transfer, according to Förster-Dexter theory, the basic condition to have Tb→Eu transfer is the spectral overlap of the acceptor absorption and the donor emission.[63] Depending on that, different η_{ET} factors have been reported; while in some examples ET is relatively low (η_{ET} ~32.3% for $[EuTb(hip)_2(H_2O)_{10},(hip),4H_2O]_\infty$[30] and 42% for $[TbEu(ip)_3(H_2O)_9{\cdot}6H_2O]_\infty$,[31] both with Tb:Eu=1), in the majority of reported cases, like in our complexes, η_{ET} >90% for Eu substitutions >10%.[27,30,60,55]

6. Static magnetic properties

Magnetization

The magnetization curves *M*(*H*) at 1.8 K measured for heteronuclear complexes of dissimilar Tb/Eu ratio **(4, 5)** collapse with that of the homonuclear Tb complex **(1)**, as shown in Fig. 7. The data could be well fitted using MAGPACK software[64] considering a model of non-interacting effective spins S^*=1/2 with uniaxial anisotropy g_z^*≈17.8(1), and a small van Vleck contribution, χ_{VV}=0.025 μ_B/kOe. As shown, at this temperature the effect of Ln-Ln' intrachain interactions is negligible.

DC susceptibility

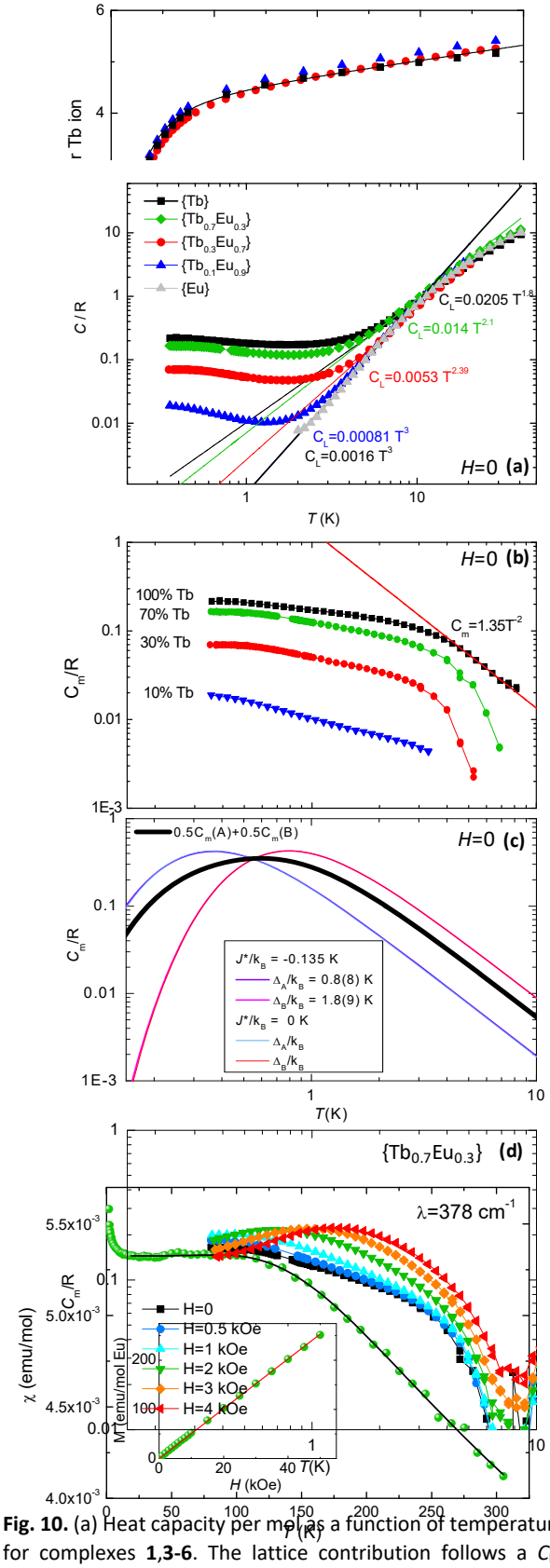

Fig. 10. (a) Heat capacity per mol as a function of temperature at *H*=0 for complexes **1**,**3**-**6**. The lattice contribution follows a $C_L/R=AT^{\alpha}$ dependence; (b) Magnetic contribution to the heat capacity at *H* = 0 for complexes **1**,**3**-**5**; (c) Simulated heat capacity for complex **1**, with an AF interaction between Tb ions J^*/k_B=-0.135 K,[47] and negligible interaction J^*/k_B=0 K; (d) Magnetic heat capacity as a function of the field for complex **3**.

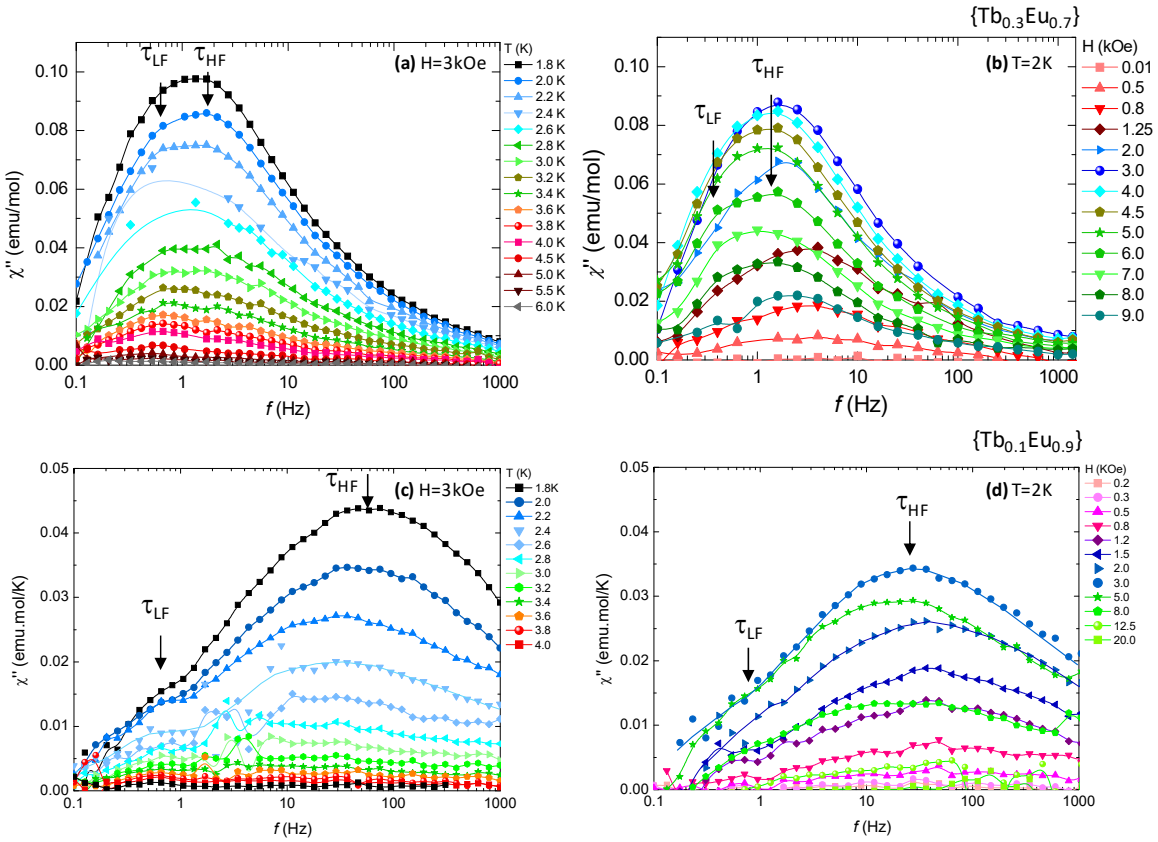

Fig. 11. $\chi''(f)$ measurements on mixed {Tb/Eu} complexes: (Top) $\{Tb_{0.3}Eu_{0.7}\}$ **(4)** and (Bottom) $\{Tb_{0.1}Eu_{0.9}\}$ **(5)**, (a)(c) at H = 3 kOe and varying temperatures, and (b)(d) at T = 2.0 K and different fields.

The dc susceptibility of the hetero compounds **(4)**, **(5)**, compared to that of homonuclear **(1)** is shown in Fig. 8. At high temperatures, while the χT product for {Tb} approaches the value $C = g_J^2 J(J+1)/8$=11.8 mol·K/emu expected for a free Tb(III) ion, for the mixed compounds χT increases and does not saturate, due to the Eu contribution. The effect is more pronounced for a compound with a larger Eu/Tb ratio, as can be observed in the $1/\chi$ vs. T plot shown in Fig. 8 (inset). By decreasing the temperature, the χT initially decreases until reaching a step value of 9.6 mol.K/emu ca. 6.4 K, and then rapidly decreases to 8.7 mol.K/emu at 1.8 K. This decrease can be explained as caused by the depopulation of the Tb Crystal Field (CF) split levels and the presence of AF intrachain interactions.[47]

The dc magnetic susceptibility χ of pure compound {Eu} **(6)** measured between 0-300 K in an applied field H=1 kOe is shown in Fig. 9. As the temperature is lowered from room temperature, χ increases smoothly tending to a plateau, of value χ(LT)=5.07×10^{-3} emu/mol, with a small increase at very low temperature, probably due to some spurious paramagnetic rare earth. Similar features have been earlier reported for Eu(III)-complexes.[65,66] It is known that in Eu(III) the ^{7}F ground term is split by the spin-orbit coupling into seven states, ^7F_J, with J taking integer values from 0 to 6, and the energies of the states are E(J)=λJ(J+1)/2, where λ is the spin-orbit constant and the energy of the $^7F_0$ ground state is taken at the origin. Given that λ is relatively small, the CF components of the first and second excited states can be thermally populated, giving rise to a paramagnetic response to the application of an external magnetic field. The experimental data could be well fitted with the theoretical isotropic equilibrium magnetic susceptibility as a function of temperature at zero field in the Van Vleck approximation:[65]

$$\chi = \frac{\sum_{J=0}^{6}(2J+1)\chi(J)\exp\left[-\lambda J(J+1)/2k_BT\right]}{\sum_{J=0}^{6}(2J+1)\exp\left[-\lambda J(J+1)/2k_BT\right]}, \qquad [3]$$

with a spin-orbit parameter of λ = 378±4 cm^{-1}. This value is in excellent agreement with that obtained from the luminescence spectrum of {Eu}, given by the energy splitting between the $^7F_0$ and the centre of gravity of the $^7F_1$ term, λ = 378.6±0.1 cm^{-1}.

Heat capacity

Fig. 10a shows the heat capacity (HC) measured at zero applied field for the mixed compounds **3-5** and homonuclear Eu complex **5** and Tb complex **1** for comparative purposes. The lattice contribution is slightly different for them and follows a $C_L/R=AT^{\alpha}$ dependence, with α=3 exponent for Eu complex and decreasing value for larger Tb contents. Concomitantly, the magnetic to lattice ratio, C_m/C_L, decreases as the percentage of Tb substitution by Eu atoms increases. The magnetic HC of all complexes is featureless down to the lowest measured temperature (T=0.35 K), and decreases proportionally to the decrease in Tb content, see Fig. 10b.

The HC data in zero field corresponds to the high temperature tail of an Ising S*=1/2 AF chain of Tb ions with negligible interaction J*, given by expression:[67]

$$C/R = \int_0^{\pi}\frac{dq}{\pi}\left(\frac{\varepsilon}{k_BT}\right)^2 \mathrm{sech}^2\left(\frac{\varepsilon}{k_BT}\right), \qquad [4]$$

per one Tb atom per formula unit, where $\varepsilon = \sqrt{(J^*/2)^2 + J^*\Delta/2\cos q + (\Delta/2)^2}$. For pure complex {Tb}, the HC data are well explained within this model assuming an equal distribution of A and B chains, including Tb atoms with "quasi-doublet" gaps Δ_A/k_B=0.8 K and Δ_B/k_B=1.8 K, respectively, (as obtained from dynamic measurements), with a small, experimentally determined intrachain AF interaction constant of J^*/k_B=-0.135 K[47].

The simulation for a negligible interaction (J^*=0) yields a similar $C_m(T)$ curve (Fig. 10c), indicating that the heat capacity in this temperature regime (0.1-10 K) is dominated by the Tb transverse gap rather than by interaction. In agreement with mentioned above, the position of the $C_m(T,H$=0) maximum for all the studied samples is not affected by dilution.

The evolution of the magnetic heat capacity as a function of the field in one of the mixed complexes, see e.g {$Tb_{0.7}Eu_{0.3}$} is shown in Fig. 10d. A maximum at low temperatures which shifts to larger values as the field increases, is observed, which is explained as the contribution due to the Zeeman splitting of the ground "quasi-doublet".

7. Dynamic magnetic properties

We studied the dynamic properties of three heterocompounds with different dilution percentage, {$Tb_{0.7}Eu_{0.3}$} **(3)**, {$Tb_{0.3}Eu_{0.7}$} **(4)** and {$Tb_{0.1}Eu_{0.9}$} **(5)**, as opposed to the previously characterized Tb-only complex **(1)**.[47]

Frequency-dependent ac measurements performed as a function of the temperature in the absence of magnetic field did not show slow relaxation of the magnetization down to the lowest reached temperature (1.8 K). Relaxation to equilibrium is likely to occur through Quantum Tunneling (QT), which is possible in such a non-Kramers compound. Notice that for {Tb} complex slow relaxation was observed, but only at very low temperatures (blocking ~0.2 K), owing to one-dimensional Single-Chain Magnet (SCM) AF behavior arising from the two types of existing chains formed by Tb(A) and Tb(B) atoms (Fig. 12a). However SCM behavior is not foreseen to occur in the diluted compounds (**2-5**).

The application of a magnetic field quenches the QT process and slow relaxation dynamics appear, as evidenced by Fig. 11(b,d), where the imaginary susceptibility curves $\chi''(f, H)$ measured at constant T=2 K are shown. χ', $\chi''(f, T)$ data were recorded in addition to the optimum field, H = 3 kOe, such that the $\chi''(f,H)_{HF}$ peak was maximum,

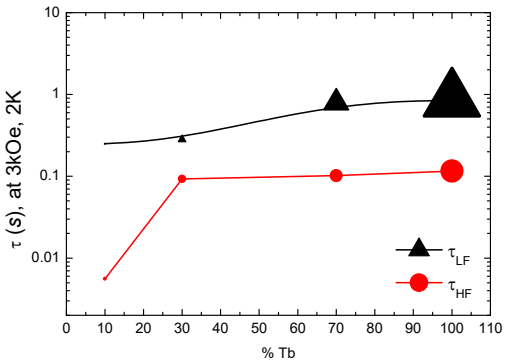

Fig. 14. (a) Dependence of the relaxation times τ_{LF} and τ_{HF}, (at H=3k Oe, T=2 K) with the % of Tb in {Tb/Eu} complexes. The size of the points is proportional to the intensity of the χ'' peaks

see Fig. 11(a,c). Two relaxation processes are observed, as evidenced by a high intensity χ'' peak at high frequencies (HF), and a smaller intensity bump at lower frequencies (LF). Comparison between the plots of complexes {$Tb_{0.3}Eu_{0.7}$} **(4)** and {$Tb_{0.1}Eu_{0.9}$} **(5)** reveals that the HF peak shifts to higher frequencies with increasing the dilution, while the position of the LF peak is practically unchanged. Results for {$Tb_{0.7}Eu_{0.3}$} **(3)**, shown in Fig. S9, follow the same trend.

The relaxation times for the two processes, τ_{LF} and τ_{HF}, as a function of the inverse temperature, $\tau(1/T)$, and as a function of the field, $\tau(H)$, have been derived from the position of the χ'' peaks and are shown in Fig. 12a and Fig. 12b, respectively. They are compared with the dependencies previously found for the pure complex {Tb} **(1)**.

The slow relaxation behavior in the {Tb/Eu} compounds cannot occur through an Orbach mechanism, as such a process would involve three energy levels and the next excited state above the "quasi-doublet" ground state is hundreds of K above. Instead, the two weakly temperature dependent slow relaxation processes observed could be explained by a two-level, direct mechanism, strongly affected by bottleneck effect (BE).

BE takes place when the energy of the lattice modes generated by the relaxing spins cannot be released into the thermal bath at sufficiently high rate.[37,68] Very slow processes affected by BE have been earlier observed in our α-fur compounds.[46,47,49] In the present

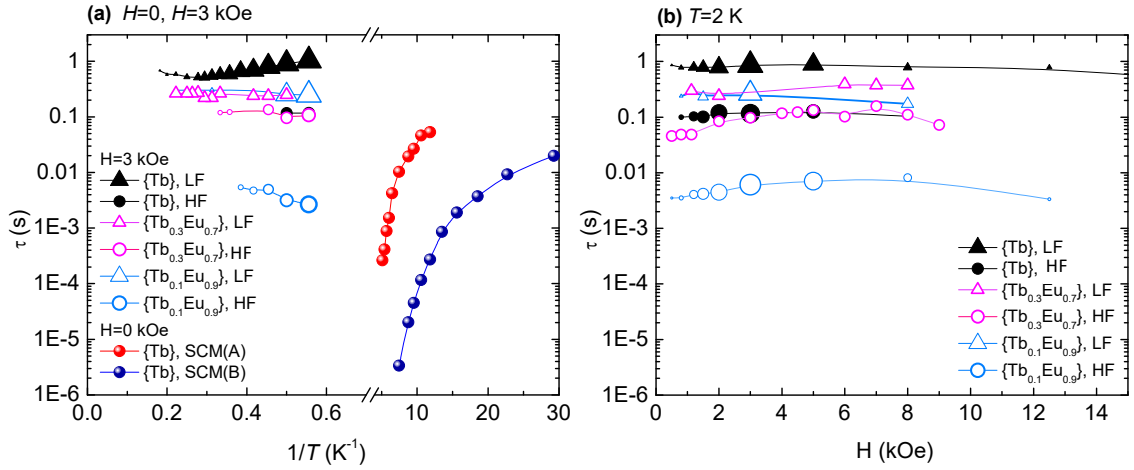

Fig. 12. (a) Relaxation time as a function of the inverse temperature at H = 0 kOe and H = 3 kOe, and (b) as a function of the applied field, at T = 2 K, for pure {Tb} **(1)** and mixed complexes {$Tb_{0.3}Eu_{0.7}$} **(4)** and {$Tb_{0.1}Eu_{0.9}$} **(5)**.

mixed {Tb/Eu} complexes, the influence of BE effect is also clear, as demonstrated by the relaxation experiments that we performed at different SQUID pressure conditions (Fig. 13), where it is appreciated that the main relaxation peak is shifted to (an order of magnitude) larger frequencies by decreasing the chamber pressure.

It is also noticeable that although these very slow relaxation processes occur in the diluted samples, they are faster than in pure {Tb}. As shown in Fig. 14, τ_{LF} decreases slowly with dilution, while τ_{HF} is reduced by more than an order of magnitude for the 10%Tb sample. The explanation might be the following: in a BE-affected direct process, the relaxation rate $\tau_{d,BE}$ depends on the intrinsic spin lattice relaxation time (τ_{sl}), the lattice-bath relaxation time (τ_{lb}), and the ratio between the heat capacity at the measured field (C_H) and the lattice heat capacity (C_L):

$$\tau_{d,BE} = \tau_{sl} + \frac{C_H}{C_l}\tau_{lb} \,. \qquad [5]$$

We have indeed observed (see Fig. 10a) that in the diluted compounds, the C_H/C_L ratio is smaller than in pure {Tb}, plausibly due to the scarcer number of Tb ions in the lattice, thus leading to the faster measured experimental rates, $\tau_{d,BE}$.

The existence of two different direct processes is unclear. It is unlikely that they correspond to two different direct processes in the two existing types of sites in the complex, Tb(A) and Tb(B), because their "quasi-doublet" gap is very similar. Moreover, both types of ions are equally present in the sample, while the intensity of one of the two observed relaxation processes is much larger than the other. A more plausible explanation, discussed by J. Flokstra *et al.*,[69, 70] is that the own relaxation process through the bath leads already to multiple peaks in χ''.

8. Conclusions

New $\{Tb_xEu_{1-x}\}$ polymeric furoate-based compounds with interesting photo-magnetic properties have been synthesized through original synthesis methods.

Luminescent studies have shown that the α-furoate ligand acts as efficient antenna group, the sensitization factor of the pure complex {Tb} being remarkably high (η_{sens}^{Tb} ~186%). For the mixed complexes, quantum yields upon ligand excitation for the pure {Tb} and {Eu} complexes, Q_{Tb}^{ligand} =23.8% (Q_{Eu}^{ligand} =7.3%) are rather typical for Tb/Eu mixed complexes. Our spectroscopic and emission lifetime analysis demonstrates there is an efficient energy transfer α-fur→Tb→Eu. The heterodinuclear strategy allows color tuning from green-to-red. Thus, these new Tb/Eu compounds could be of interest as luminescent agents.

From the magnetic point of view, the structure of the {Tb} complex is formed by Ising S*=1/2 chains of weakly interacting (J'/k_B=-0.135 K) non-Kramer ions.[47] In the diluted compounds, Eu ions break this structure into segments of different length. The static magnetization at 1.8 K is well explained by this Ising model, with negligible interaction at this temperature.

The dynamical study of the 10%, 30% and 70% Tb complexes has shown that in H = 0 fast relaxation occurs, as the non-Kramers character of the Tb ion favors the quantum tunneling process through the ground "quasi-doublet". At $H \neq 0$ tunneling is quenched and two slow relaxation pathways open up. The very small relaxation times observed are assigned to direct processes, affected by BE, as earlier observed in other furoate compounds. Magnetic dilution has the effect of speeding up the two direct processes by one-two orders of magnitude, respectively, as compared to the pure Tb complex, as a result of the decreasing magnetic-to-lattice contribution in the Tb/Eu complexes.

In conclusion, the synthesized mixed $\{Tb_xEu_{1-x}(\alpha\text{–fur})_3(H_2O)_3\}_n$ 1D polymers represent a new family of interesting multifunctional materials combining tunable luminescent and SMM properties

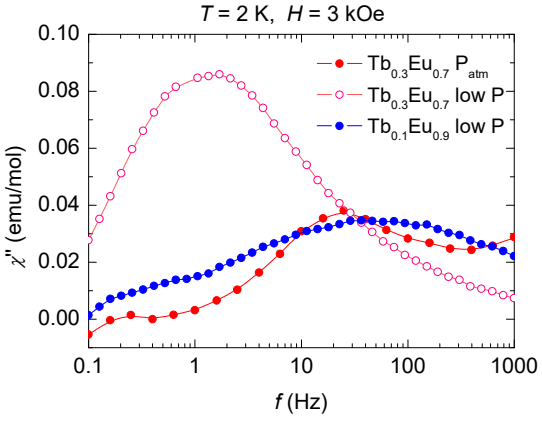

Fig. 13. $\chi''(f)$ measurements on mixed {Tb/Eu} complexes: (Top) $\{Tb_{0.3}Eu_{0.7}\}$ (**4**) and $\{Tb_{0.1}Eu_{0.9}\}$ (**5**) in different experimental SQUID pressure conditions.

Acknowledgements

This work has been financed by MINECO Project MAT2017-83468-R and MINECO)/FEDER (Project CTQ2015-67461-P). Authors would like to acknowledge the use of *Servicio General de Apoyo a la Investigación*-SAI, Universidad de Zaragoza. D.P. is supported by the Critical Materials Institute, an Energy Innovation Hub funded by the U.S. Department of Energy, Office of Energy Efficiency and Renewable Energy, Advanced Manufacturing Office. The financial support of European Social Fund for Regional Development, Competitiveness Operational Programme Axis 1 – Project "Novel Porous Coordination Polymers with Organic Ligands of Variable Length for Gas Storage", POCPOLIG (ID P_37_707, Contract 67/08.09.2016, cod MySMIS: 104810) is gratefully acknowledged by Dr. Shova.

References

1 J. Bartolomé, F. Luis and J. F. Fernández, Eds., *Molecular Magnets*, Springer, 2014.

2 R. Sessoli and A. K. Powell, *Coord. Chem. Rev.*, 2009, **253**, 2328–2341.

3 R. A. Layfield and M. Murugesu, *Lanthanides and actinides in Molecular magnetism*, Wiley-VCH, 2015.

4 E. Bartolomé, A. Arauzo, J. Luzón, J. Bartolomé and F. Bartolomé, in *Handbook of Magnetic Materials*, ed. E. Brück, Elsevier, 2017, pp. 1–289.

5 G. C. G. Bünzli and C. Piguet, *Chem. Soc. Rev.*, 2005, **34**, 1048–1077.

6 B. Sieklucka and D. Pinkowicz, Eds., *Molecular Magnetic Materials*, Wiley-VCH Verlag GmbH, Weinheim, Germany, 2017.

7 S. V. Eliseeva and J.-C. G. Bünzli, *Chem. Soc. Rev.*, 2010, **39**, 189–227.

8 D. Prodius and A.-V. Mudring, *Coord. Chem. Rev.*, 2018, **363**, 1–16.

9 P. Zhang, Y. N. Guo and J. Tang, *Coord. Chem. Rev.*, 2013, **257**, 1728–1763.

10 N. Ishikawa, M. Sugita, T. Ishikawa, S. Y. Koshihara and Y. Kaizu, *J. Am. Chem. Soc.*, 2003, **125**, 8694–8695.

11 P. Robaschik, M. Fronk, M. Toader, S. Klyatskaya, F. Ganss, P. F. Siles, O. G. Schmidt, M. Albrecht, M. Hietschold, M. Ruben, D. R. T. Zahn and G. Salvan, *J. Mater. Chem. C*, 2015, **3**, 8039–8049.

12 M. Urdampilleta, S. Klyatskaya, M. Ruben and W. Wernsdorfer, *ACS Nano*, 2015, **9**, 4458–4464.

13 Y. Horii, Y. Horie, K. Katoh, B. K. Breedlove and M. Yamashita, *Inorg. Chem.*, 2018, **57**, 564–574.

14 C. R. Ganivet, B. Ballesteros, G. de la Torre, J. M. Clemente-Juan, E. Coronado and T. Torres, *Chem. - Eur. J.*, 2013, **19**, 1457–1465.

15 S. Osa, T. Kido, N. Matsumoto, N. Re, A. Pochaba and J. Mrozinski, *J. Am. Chem. Soc.*, 2004, **126**, 420–421.

16 J. D. Rinehart, M. Fang, W. J. Evans and J. R. Long, *J. Am. Chem. Soc.*, 2011, **133**, 14236–14239.

17 N. Ishikawa, T. Iino and Y. Kaizu, *J. Am. Chem. Soc.*, 2002, **124**, 11440–11447.

18 R. J. Holmberg, M. A. Polovkova, A. G. Martynov, Y. G. Gorbunova and M. Murugesu, *Dalton Trans.*, 2016, **45**, 9320–9327.

19 R. Sato, K. Suzuki, M. Sugawa and N. Mizuno, *Chem. -Eur. J.*, 2013, **19**, 12982–12990.

20 F. Luis, A. Repollés, M. J. Martínez-Pérez, D. Aguilà, O. Roubeau, D. Zueco, P. J. Alonso, M. Evangelisti, A. Camón, J. Sesé, L. A. Barrios and G. Aromí, *Phys. Rev. Lett.*, 2011, **107**, 117203–117208.

21 D. Aguilà, L. A. Barrios, V. Velasco, O. Roubeau, A. Repollés, P. J. Alonso, J. Sesé, S. J. Teat, F. Luis and G. Aromí, *J. Am. Chem. Soc.*, 2014, **136**, 14215–14222.

22 G. Aromí, D. Aguilà, P. Gamez, F. Luis and O. Roubeau, *Chem. Soc. Rev.*, 2012, **41**, 537–546.

23 D. Aguilà, L. A. Barrios, F. Luis, A. Repollés, O. Roubeau, S. J. Teat and G. Aromí, *Inorg. Chem.*, 2010, **49**, 6784–6786.

24 R. Ilmi and K. Iftikhar, *Inorg. Chem. Commun.*, 2012, **20**, 7–12.

25 I. Oyarzabal, B. Artetxe, A. Rodríguez-Diéguez, J. A. García, J. M. Seco and E. Colacio, *Dalton Trans.*, 2016, **45**, 9712–9726.

26 Y. C. Miranda, L. L. A. L. Pereira, J. H. P. Barbosa, H. F. Brito, M. C. F. C. Felinto, O. L. Malta, W. M. Faustino and E. E. S. Teotonio, *Eur. J. Inorg. Chem.*, 2015, 3019–3027.

27 Y. Luo, G. Calvez, S. Freslon, K. Bernot, C. Daiguebonne and O. Guillou, *Eur. J. Inorg. Chem.*, 2011, 3705–3716.

28 F. Artizzu, F. Quochi, A. Serpe, E. Sessinin and P. Deplano, *Inorg. Chem.*, 2015, **2**, 213–222.

29 S. Freslon, Y. Luo, C. Daiguebonne, G. Calvez, K. Bernot and O. Guillou, *Inorg. Chem.*, 2016, **55**, 794–802.

30 X. Fan, S. Freslon, C. Daiguebonne, G. Calvez, L. Le Pollès, K. Bernot and O. Guillou, *J. Mater. Chem. C*, 2014, **2**, 5510–5525.

31 S. Freslon, Y. Luo, G. Calvez, C. Daiguebonne, O. Guillou, K. Bernot, V. Michel and X. Fan, *Inorg. Chem.*, 2014, **53**, 1217–1228.

32 X. Zhou, L. Chen, Z. Feng, S. Jiang, J. Lin, Y. Pang, L. Li and G. Xiang, *Inorg. Chim. Acta*, 2018, **469**, 576–582.

33 P. Xiao, P. Wang, R. Q. Fan, X. Du, W. Chen, H. J. Zhang, Y. Song and Y. L. Yang, *RSC Adv.*, 2016, **6**, 83091–83100.

34 Z. F. Liu, M. F. Wu, S. H. Wang, F. K. Zheng, G. E. Wang, J. Chen, Y. Xiao, A. Q. Wu, G. C. Guo and J. S. Huang, *J. Mater. Chem. C*, 2013, **1**, 4634–4639.

35 Z. V. Dobrokhotova, S. P. Petrosyants, A. B. Ilyukhin, Y. S. Zavorotny, V. I. Gerasimova, Y. A. Mikhlina, N. N. Efimov and V. M. Novotortsev, *Inorganica Chim. Acta*, 2017, **456**, 76–85.

36 I. G. Fomina, Z. V. Dobrokhotova, A. B. Ilyukhin, V. I. Zhilov, A. S. Bogomyakov, A. A. Antoshkov, Y. S. Zavorotny, V. I. Gerasimova, V. M. Novotortsev and I. L. Eremenko, *Dalton Trans.*, 2014, **43**, 18104–18116.

37 Q. Li, T. Li and J. Wu, *J.Phys. Chem. B*, 2001, **105**, 12293–12296.

38 D. T. de Lill, A. de Bettencourt-Dias and L. Cahill, *Inorg. Chem.*, 2007, **46**, 3960–3965.

39 I. G. Fomina, Z. V. Dobrokhotova, G. G. Aleksandrov, V. I. Zhilov, I. P. Malkerova, A. A.S., D. M. Zhigunov, A. S. Bogomyakov, V. I. Gerasimova, V. M. Novotortsev and I. L. Eremenko, *Polyhedron*, 2013, **50**, 297–305.

40 E. Chelebaeva, J. Long, J. Larionova, R. A. S. Ferreira, L. D. Carlos, F. A. Paz, J. B. R. Gomes, A. Trifonov, C. Guerin and Y. Guari, *Inorg. Chem.*, 2012, **51**, 9005−9016.

41 E. F. Schubert, *Light Emitting Diodes*, Cambridge University Press, New York, 2006.

42 W.-H. Zhu, X. Xiong, C. Gao, S. Li, Y. Zhang, J. Wang, C. Zhang, A. K. Powell and S. Gao, *Dalton Trans.*, 2017, **46**, 14114–14121.

43 Y. Bi, X. T. Wang, W. Liao, X. Wang, R. Deng, H. Zhang and S. Gao, *Inorg. Chem.*, 2009, **48**, 11743–11747.

44 X. Wei, L.-Y. Yang, S.-Y. Liao, M. Zhang, J.-L. Tian, P.-Y. Du, W. Gu and X. Liu, *Dalton Trans.*, 2014, **43**, 5793–5800.

45 C. Boskovic, *Acc. Chem. Res.*, 2017, **50**, 2205–2214.

46 E. Bartolomé, J. Bartolomé, S. Melnic, D. Prodius, S. Shova, A. Arauzo, J. Luzón, F. Luis and C. Turta, *Dalton Trans.*, 2013, **42**, 10153–10171.

47 E. Bartolomé, J. Bartolomé, A. Arauzo, J. Luzón, L. Badía, R. Cases, F. Luis, S. Melnic, D. Prodius, S. Shova and C. Turta, *J. Mater. Chem. C*, 2016, **4**, 5038–5050.

48 C. Turta, S. Melnic, M. Bettinelli, S. Shova, C. Benelli, A. Speghini, A. Caneschi, M. Gdaniec, Y. Simonov, D. Prodius and V. Mereacre, *Inorg. Chim. Acta*, 2007, **360**, 3047–3054.

49 E. Bartolomé, J. Bartolomé, S. Melnic, D. Prodius, S. Shova, A. Arauzo, J. Luzón, L. Badía-Romano, F. Luis and C. Turta, *Dalton Trans.*, 2014, **43**, 10999–11013.

50 G. Wyszecky and W. S. Stiles, *Color science: Concepts and methods, quantitative data and formulae*, John Wiley and Sons, New York, 1982.

51 D. Prodius, C. Turta, V. Mereacre, S. Shova, M. Gdaniec, Y. Simonov, J. Lipkowski, V. Kuncser, G. Filoti and A. Caneshi, *Polyhedron*, 2006, **25**, 2175–2182.

52 C. I. Turta, D. N. Prodius, V. M. Mereacre, S. G. Shova, M. Gdaniec, Y. A. Simonov, V. Kuncser, G. Filoti, A. Caneshi and L. Sorace, *Inorg. Chem. Commun.*, 2004, **7**, 576–579.

53 V. Mereacre, D. Prodius, C. Turta, S. Shova, G. Filoti, J. Bartolomé, R. Clérac, C. E. Anson and A. K. Powell, *Polyhedron*, 2009, **28**, 3017–3025.

54 J. Bartolomé, G. Filoti, V. Kuncser, G. Schinteie, V. Mereacre, C. E. Anson, A. K. Powell, D. Prodius and C. Turta, *Phys. Rev.*

B, 2009, **80**, 014430.
55 L. Badía-Romano, F. Bartolomé, J. Bartolomé, J. Luzón, D. Prodius, C. Turta, V. Mereacre, F. Wilhelm and A. Rogalev, *Phys. Rev. B*, 2013, **87**, 184403–184414.
56 L. Badía-Romano, J. Rubín, F. Bartolomé, J. Bartolomé, J. Luzón, D. Prodius, C. Turta, V. Mereacre, F. Wilhelm and A. Rogalev, *Phys. Rev. B*, 2015, **92**, 064411–064424.
57 L. Badía-Romano, J. Rubín, F. Bartolomé, J. Bartolomé, J. Luzón, D. Prodius, C. Turta, V. Mereacre, F. Wilhelm and A. Rogalev, *J. Magn. Magn. Mater.*, 2016, **400**, 137–140.
58 C. Turta, S. Melnic, M. Bettinelli, S. Shova, C. Benelli, A. Speghini, A. Caneschi, M. Gdaniec, Y. Simonov, D. Prodius and V. Mereacre, *Inorg. Chim.*, 2007, **360**, 3047–3054.
59 K. Binnemans, *Coord. Chem. Rev.*, 2015, **295**, 1–45.
60 M. O. Rodrigues, J. D. L. Dutra, L. A. O. Nunes, G. F. de Sá, W. M. de Azevedo, P. Silva, F. A. A. Paz, R. O. Freire and A. Severino, *J.Phys.Chem.C*, 2012, **116**, 19951–19957.
61 N. Kerbellec, D. Kustaryono, V. Haquin, M. Etienne, C. Daiguebonne and O. Guillou, *Inorg. Chem.*, 2009, **48**, 2837–2843.
62 V. Haquin, F. Gumy, C. Daiguebonne, J. C. G. Bünzli and O. Guillou, *Eur.J.Inorg.Chem.*, 2009, 491–497.
63 S. Speiser, *Chem.Rev.*, 1996, **96**, 1953–1976.
64 E. Ramos, J. E. Roman, S. Cardona-Serra and J. M. Clemente-Juan, *Comput. Phys. Commun.*, 2010, **181**, 1929–1940.
65 M. Andruh and P. Porchers, *Luminescence*, 1993, 1616–1622.
66 A. Arauzo, A. Lazarescu, S. Shova, E. Bartolomé, R. Cases, J. Luzón, J. Bartolomé and C. Turta, *Dalton Trans.*, 2014, **43**, 12342–12356.
67 S. Katsura, *Phys. Rev.*, 1962, **127**, 1508–1518.
68 R. R. Schenker, M. N. Leuenberger, G. Chaboussant, D. Loss and H. U. Güdel, *Phys. Rev. B Condens. Matter*, 2005, **72**, 184403–184413.
69 G. J. Gerritsma, J. Flokstra, G. A. Hartemink, J. J. M. Scholten, A. J. W. A. Vermeulen and L. C. van der Marel, *Phys. B&C*, 1978, **95**, 173–182.
70 J. Flokstra, G. J. Gerritsma, G. A. Hartemink and L. C. van der Marel, *Physica*, 1974, **77**, 99–120.